

Ultrasensitive Molecular Sensors Based on Real-Time Impedance Spectroscopy in Solution-Processed 2D Materials

David C. Moore, Ali Jawaid, Robert Busch, Michael Brothers, Paige Miesle, Adam Miesle, Rahul Rao, Jonghoon Lee, Lucas K. Beagle, Michael Motala, Shay Goff Wallace, Julia R. Downing, Ajit Roy, Christopher Muratore, Mark C. Hersam, Richard Vaia, Steve Kim, and Nicholas R. Glavin*

Chemical sensors based on solution-processed 2D nanomaterials represent an extremely attractive approach toward scalable and low-cost devices. Through the implementation of real-time impedance spectroscopy and development of a three-element circuit model, redox exfoliated MoS₂ nanoflakes demonstrate an ultrasensitive empirical detection limit of NO₂ gas at 1 ppb, with an extrapolated ultimate detection limit approaching 63 ppt. This sensor construct reveals a more than three orders of magnitude improvement from conventional direct current sensing approaches as the traditionally dominant interflake interactions are bypassed in favor of selectively extracting intraflake doping effects. This same approach allows for an all solution-processed, flexible 2D sensor to be fabricated on a polyimide substrate using a combination of graphene contacts and drop-casted MoS₂ nanoflakes, exhibiting similar sensitivity limits. Finally, a thermal annealing strategy is used to explore the tunability of the nanoflake interactions and subsequent circuit model fit, with a demonstrated sensitivity improvement of 2× with thermal annealing at 200 °C.

sition metal dichalcogenides (TMDs), including 2D molybdenum disulfide (MoS₂), have drawn much interest in the sensing community, especially for analytes such as NO₂ and NH₃ that are known to alter the electrical conductivity of TMDs via doping.^[3–5] Electronic sensors traditionally involve a simple two-terminal electronic device with MoS₂ as a channel material,^[6] where molecular binding events within the semiconducting channel alter the direct current (DC) conductivity.^[7] The detection limits for MoS₂ and other TMDs integrated into DC sensor devices, however, tend to be limited to the ppm range,^[6,9–11] which is insufficient for detecting harmful gases at hazardous exposure limits such as NO₂ (1 ppm), CS₂ (1 ppm), and naphthalene (0.1 ppm). Various strategies have been implemented to lower the detection threshold, which have mainly focused on creating heterostructures or other novel material configurations,^[4,12–20] using photon excitation, surface acoustic waves, or electrical resistance sensitivity enhancement through field-effect transistors,^[21–23] Schottky diodes,^[24,25] conductometrics,^[26,27] or some combination thereof.^[28,29] Of these strategies, photoexcitation has demonstrated the most promise, with resultant sensors

1. Introduction

The high surface to volume ratio, tunable surface chemistry, and exceptional electronic properties of 2D materials have resulted in chemical gas sensor devices with some of the highest sensitivities of any material class to date.^[1,2] Semiconducting tran-

D. C. Moore, A. Jawaid, R. Busch, P. Miesle, A. Miesle, R. Rao, J. Lee, L. K. Beagle, M. Motala, A. Roy, R. Vaia, N. R. Glavin
Materials and Manufacturing Directorate
Air Force Research Laboratory
Wright-Patterson AFB, OH 45433, USA
E-mail: Nicholas.Glavin.1@us.af.mil

D. C. Moore, A. Jawaid, R. Busch, M. Brothers, P. Miesle, A. Miesle, L. K. Beagle, M. Motala
UES Inc.
Dayton, OH 45432, USA

 The ORCID identification number(s) for the author(s) of this article can be found under <https://doi.org/10.1002/adfm.202106830>.

DOI: 10.1002/adfm.202106830

M. Brothers, S. Kim
711th Human Performance Wing
Air Force Research Laboratory
Wright-Patterson AFB, OH 45433, USA

J. Lee
Universal Technology Corporation
Dayton, OH 45432, USA

S. G. Wallace, J. R. Downing, M. C. Hersam
Department of Materials Science and Engineering
Northwestern University
Evanston, IL 60208, USA

C. Muratore
Department of Chemical and Materials Engineering
University of Dayton
Dayton, OH 45469, USA

demonstrating an ultimate detection limit of NO₂ at sub ppb levels.^[3,30–33]

Simple device architectures incorporating solution-processed materials without the requirement for photoexcitation create a paradigm shift in the design of low cost sensors, where techniques including additive manufacturing and flow coating can take advantage of high volume production and scale-up for industrial purposes.^[34] Additionally, solution-processable 2D nanoflake architectures provide extremely high surface area to volume ratios, with the vapor having access to both surface and edge sites.^[35–38] Liquid-phase electrochemical impedance spectroscopy, where measurement of AC frequency sweeps and subsequent modeling to create a physical equivalent circuit, is a common technique in liquid electrolytes^[39–42] including 2D materials.^[35] Impedimetric sensors^[43–45] and even full frequency sweeps with equivalent circuits^[46] have also been employed in gas sensing, but have yet to be used with solution-processed nanoflakes in a practical sensor configuration. Furthermore, both electrochemical activity and resonance methods typically

rely upon analyte-active phenomena that are not necessary in the presented method. Herein, we present a technique to increase the detection threshold by three orders of magnitude for solution-processed MoS₂ nanoflakes via real-time measurement of impedance without the requirement of photoexcitation or thermal annealing, which can be deleterious to wearable platforms.^[47]

2. Results and Discussion

The few-layer TMD nanoflakes used in this work were exfoliated from bulk powders using the redox exfoliation process and dispersed in acetonitrile.^[48–50] The dispersions contain of few-layer MoS₂ flakes with a strong optical absorbance peak at 669 nm (1.85 eV), an average flake diameter of 100 nm, and a thickness of 2–8 layers (Figure 1a,b). The acetonitrile/MoS₂ dispersions were flow-coated (depicted in Figure 1c) onto a Si/SiO₂ substrate with patterned Ti/Au contacts (10 nm

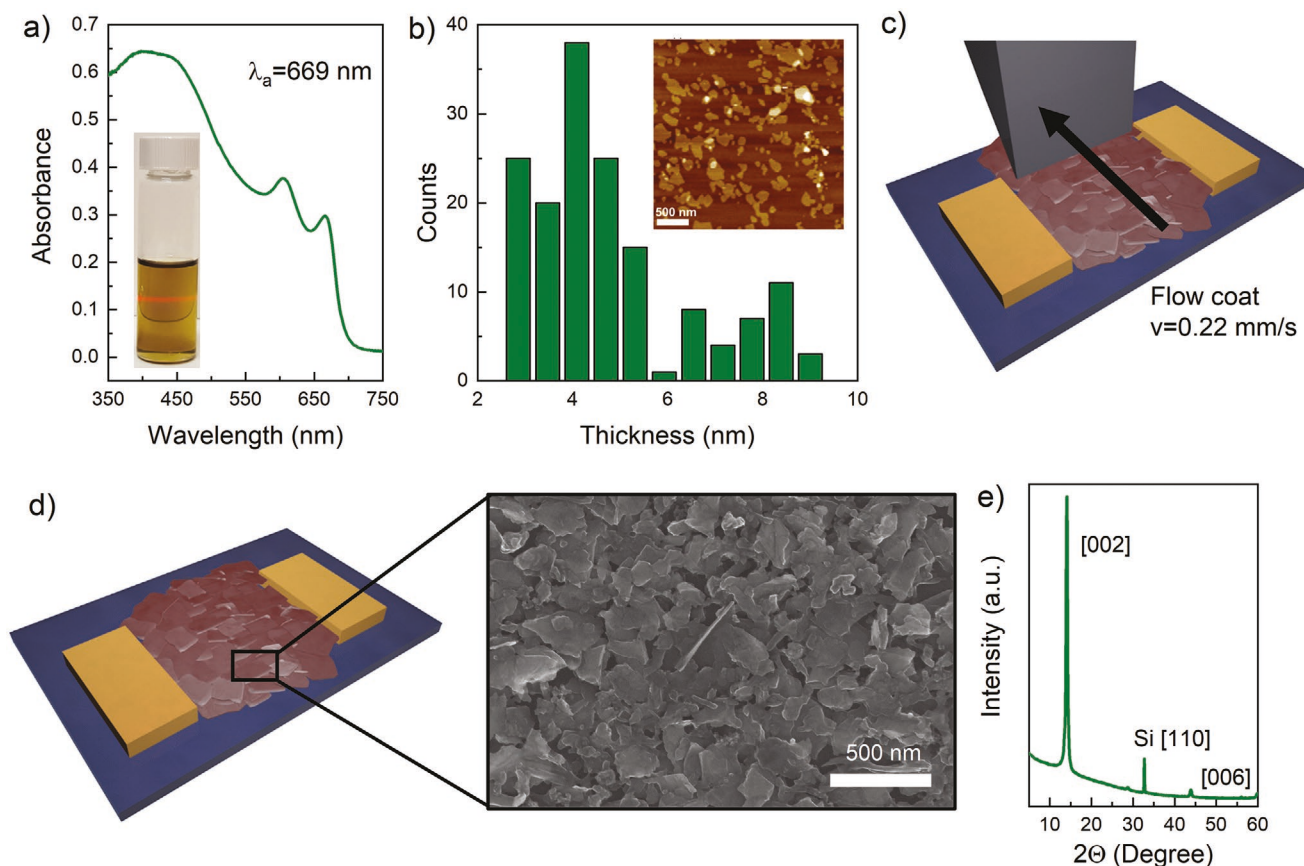


Figure 1. Morphology analysis of MoS₂ nanoflake films. a) UV-vis absorption spectrum of MoS₂ flakes used for film deposition. Direct bandgap is observed at 669 nm, indicating the dispersion is rich in few-to-monolayer populations. Inset: Optical image of diluted dispersion. b) Height analysis of MoS₂ flakes indicating that the average height of each flake is 4.0 ± 1.2 nm. Typical step heights of flakes obtained from the redox exfoliation method are generally 1.5–2 nm, indicating the individual flakes are typically 1–3 layers in the films analyzed in this study and inset depicts AFM image of MoS₂ flakes on Si, showing 100–200 nm lateral size, flat materials. Note: The particles imaged in AFM are from dilute, discontinuous deposition to identify single flake morphology whereas films deposited for sensing measurements were continuous and cohesive. c) Schematic of thin film preparation. A solution of MoS₂ in acetonitrile (3 mg mL^{-1}) is applied to a blade and sheared on the surface of the substrate. The resulting deposited MoS₂ assembles along the 002 crystallographic axis, where the thickness of films can be controlled via the deposition velocity. Ka of X-ray analysis direction is shown in pictograph of assembled film. d) SEM top-side view of obtained films indicate highly oriented MoS₂ films. e) XRD spectra of thin films indicating preferred orientation deposited along the 00/ crystallographic axis. The absence of in-plane reflectance indicates preferred orientation parallel to the substrate.

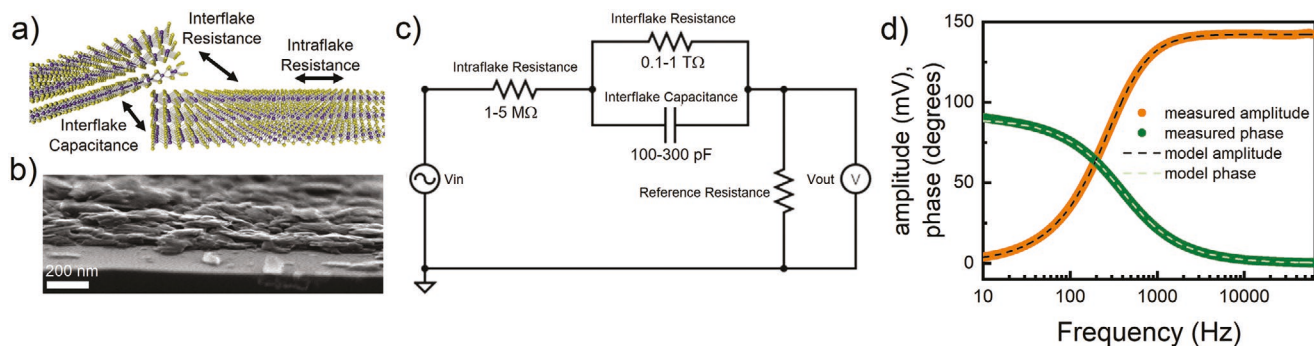


Figure 2. Nanoflake real-time impedance monitoring sensor model. a) Schematic of flake interactions including interflake resistance, intraflake resistance, and interflake capacitance. b) Cross-sectional SEM of aligned nanoflake film, c) circuit diagram, and d) frequency sweep with both measured and modeled phase and amplitude.

Ti/50 nm Au) separated by a channel length of 100 μm . The flow coating was performed at a velocity of 0.22 mm s^{-1} to form cohesive thin films of that are 80–100 nm in thickness (Figure 1d). The flow-coated process induces mostly horizontally aligned flakes with crystallographic orientation on the 002 axis as shown in the scanning electron microscope (SEM) image in Figure 1d and X-ray diffraction (XRD) pattern in Figure 1e.

Initial DC resistance measurements of the as-deposited flow-coated MoS_2 films (further information in Figure S1 in the Supporting Information) revealed very high resistance values approaching more than 100 $\text{G}\Omega$, attributed to the large contact resistance at the flake-to-flake interfaces. In order to overcome this limitation, an impedance approach outlined in this work conceptualizes the nanoflake network as multiple circuit elements both in series and parallel. As shown in Figure 2a,b, each nanoflake exhibits a combination of resistances and capacitances to include in-plane resistance (intraflake resistance, R_{intra}), resistance between flakes (interflake resistance, R_{inter}), and pseudoparallel plate capacitance between adjacent flakes (interflake capacitance, C_{inter}). The resultant impedance properties within the film can be reduced to the model depicted in Figure 2c based on the real time fitting of the amplitude and phase in the range of 10 Hz to 50 kHz (Figure 2d). A more detailed description of the impedance circuit model and the fitting can be found in the Supporting Information.

Theoretical and empirical work on electron transport in 2D materials tends to focus on DC current, where both edge and plane states play a significant role.^[51] However, in the proposed model, the plane and edge current would be encompassed within the intraflake phenomena, and leakage current and soakage of the interflake capacitances would be subsumed into interflake resistance and intraflake resistance, respectively. Thus, the interflake capacitance may be considered approximately ideal, that is, all capacitive current is induced current. It is therefore assumed that while the 2D semiconductor flakes interact with ambient vapor phase species, intraflake resistance is affected primarily by the number of available charge carriers, and interflake resistance by planar tunneling over van der Waals gaps. Due to limitations of the model, junction resistances, such as a Schottky barrier, would also be modeled within the intraflake resistance. The interflake capacitance is believed

to be mostly affected by the interflake distances and the dielectric constant of the environment.^[52]

To further investigate the underlying transport mechanisms of the MoS_2 nanoflake film, electrical resistance of the film was measured over a range of temperatures from room temperature to 120 $^{\circ}\text{C}$. Both the variable range hopping (VRH)^[53–55] and band-like transport mechanisms^[56,57] have been used to describe electron flow in films of graphene and MoS_2 , with transition to band-like transport in highly crystalline flakes. In this case, the lack of clear dominant carrier mechanism in the featured Arrhenius type behavior of the temperature-dependent electrical conductivity (further details in Figure S5 in the Supporting Information) indicates that, in accordance with the proposed responses from inter- and intraflake conductivity, most likely neither transport mode dominates the electronic conductivity.

The real-time impedance monitored sensor performance as a function of concentration of NO_2 gas is shown in Figure 3a, with a clear opposite trend observed for the value of intraflake resistance and interflake capacitance. The resistance response to NO_2 indicates p-type behavior,^[58] which has been observed in solution-processed TMDs due to surface doping effects, notably oxygen incorporation.^[59–61] MoS_2 is typically n-type due to prevalence of sulfur vacancies,^[62–64] but X-ray photoelectron spectroscopy (XPS) of the sensor materials revealed a large increase in Mo^{6+} due to oxidation to MoO_3 in tested materials over newly exfoliated samples (see the Supporting Information for details). The oxidation to MoO_3 was likely accelerated in the aged samples by the prevalence of edge sites in the nanoflakes. It is important to note that Fermi level pinning from contacts on MoS_2 can also induce p-type behavior^[65] and is known to be complicated by both Mo and S interactions,^[66] defects and impurities in the MoS_2 lattice,^[67,68] surface defects on the gold,^[69] or inclusions of MoO_3 .^[70] Additionally, molybdenum oxides tends to be highly hygroscopic, which may complicate the response, however, an overnight purge of nitrogen before sensor testing ensured minimal contributions from water or adsorbates prior to the testing and the sensor response upon exposure to water was also minimal (more details in Figure S12 in the Supporting Information).^[71] While the oxidation of MoS_2 nanoflakes presumably contributes to the p-type behavior in the sensor response, the stability of the sensor devices is unaffected, as the resistance response is robust and stable over

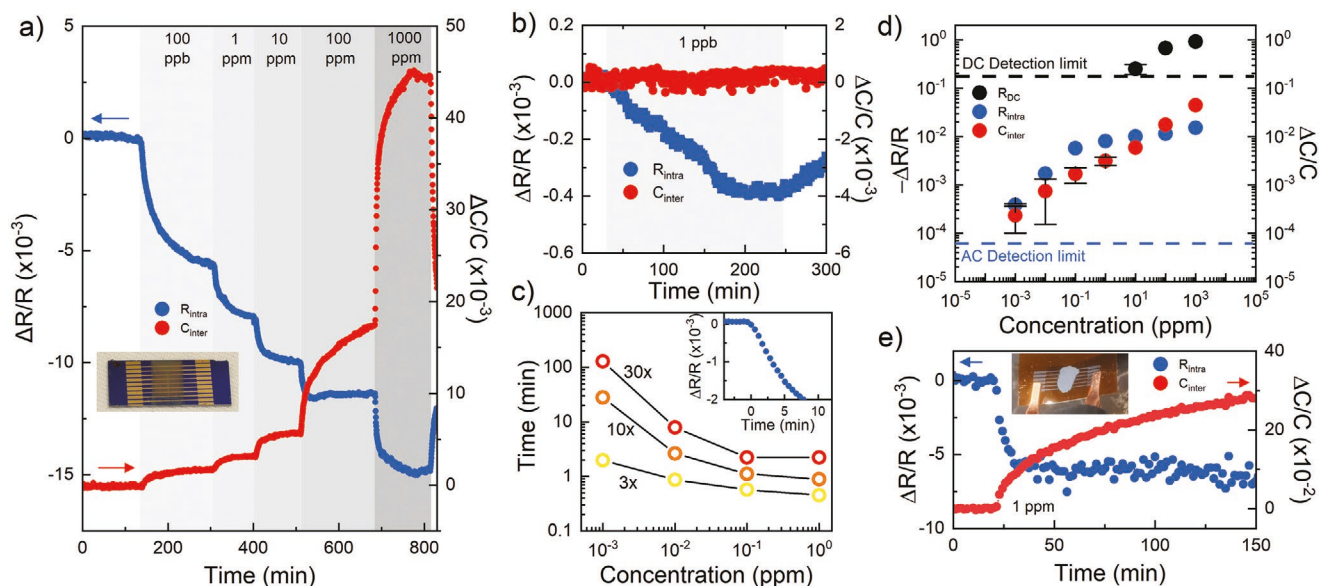


Figure 3. Real-time impedance spectroscopy sensor results for NO₂ detection. a) Resistance and capacitance response at various NO₂ concentrations with inset image of flow-coated MoS₂ nine-channel sensor device, b) 1 ppb NO₂ response, c) concentration-dependent noise threshold with inset of initial sensor trigger, d) equilibrium $\Delta R/R$ and $\Delta C/C$ for various circuit elements with detection limits identified based on signal to noise ratio, and e) demonstrated flexible device with inset image of drop-casted MoS₂ flakes onto printed graphene electrodes.

15 months of aging and testing (further details in Figure S6 in the Supporting Information).

The impedance approach developed in this work exhibits remarkable signal fidelity with low signal to noise, and empirically detects NO₂ gas as low as 1 ppb (Figure 3b). This value represents one of the lowest detectable NO₂ concentrations to date, as several previous studies have extrapolated to detect to sub ppb levels but none of which are solution processable and in a simple electronic chemiresistor device configuration.^[6] The extrapolated detection limit of the unannealed nanoflake sensors in this study is 63 ppt with a 95% confidence interval from 38 to 94 ppt (further details in Figure S8 in the Supporting Information). The time-dependent response shown in Figure 3c indicates that full saturation of the electronic signature is slow, which is common in nanoflake chemical sensors and presumably from diffusion limitations.^[72] The initial sensor response, however, is rapid enough to be viable for real-world sensor applications that recommend a maximum exposure of 1 ppm over several minutes or 3 ppm over a period of 8 h. To demonstrate this, we incorporated a simulated trip condition for various multiples (3 \times , 5 \times , and 10 \times) of the noise threshold, as shown in Figure 3c, which indicate that the detection threshold can be reached on the order of seconds for concentrations near health hazard levels, and only minutes into the ppb range.

The low AC signal noise enables an exceptionally low signal threshold compared to the same devices under DC evaluation, as shown in Figure 3d. Both R_{intra} and C_{inter} have dimensionless thresholds of 0.00006 and 0.0004, respectively, which allows for a theoretical limit of 63 ppt for R_{intra} and 2.6 ppb for C_{inter} (more detail in the Supporting Information). With the large contact resistance between nanoflakes, the DC resistance is high, reducing the detection threshold as the noise begins to dominate the signal for lower concentrations (further details in Figure S7 in the Supporting Information). Both C_{inter} and R_{intra}

fit linearly to the log–log graph, suggesting a Freundlich adsorption isotherm, which is typical for lower concentrations^[73] and has been observed on similar materials.^[20] The concentration profile for R_{intra} in Figure 3d has two regimes, with an increased slope at concentrations below 100 ppb that eventually saturates and becomes a power relation, as opposed to the capacitance that does not saturate. We attribute this difference in signal to a physical difference in the mechanism of parallel resistance and capacitance, where at low concentrations, the data adheres well to the Freundlich model. This is likely due to the edge sites and basal planes saturating at different rates, thus changes the adsorption constant. The vertical profile of the film is analogous to parallel elements, and due to the reciprocal sum of reciprocals law, the lowest resistor in a parallel grouping will dominate the signal whereas capacitance will add linearly. Thus, as the top layer interacts with the analyte to reduce R_{intra} , it saturates at lower concentrations. Additionally, these devices demonstrate performance stability with long-term exposure to permanent gases that behave as dopants (more detail in Figure S6 in the Supporting Information), with the device used to evaluate the 1 ppb curve in Figure 3b being over six months old and involved in over a dozen tests of various analytes. Although desorption under nitrogen is slow (more detail in Figure S10 in the Supporting Information), the device fully recovers under storage in argon, with a decrease in sensitivity of 25–27% observed from initial test to subsequent tests over the course of more than a year.

To further demonstrate the versatility of the described approach, an all solution-processed 2D material sensor was developed comprising of printed graphene contacts with drop-casted MoS₂ nanoflakes on a flexible polyimide substrate, as shown in Figure 3e. The printed sensor demonstrated a detection of 1 ppm NO₂ easily realized in both the R_{intra} and C_{inter} (Figure 3e) and presents comparable performance to the devices

on the silicon substrate. In this configuration, both the baseline R_{intra} and ΔR_{inter} became far more significant. We attribute this to the drop-casting technique resulting in less laminar orientation relative to the flow-coating technique, resulting in more transverse current flow. This device further demonstrates the advantage of the real-time impedance sensor method for solution-processed 2D materials and the potential for inexpensive, modular wearable sensors.

To explore the influence of crystalline defects on sensor performance, the nanoflake sensors were exposed to a step-wise thermal annealing study. The annealing was performed in vacuum (10^{-6} Torr) and was followed with characterization by resonant Raman spectroscopy (633 nm excitation) to investigate structural changes in the TMD nanoflakes in conjunction with both AC and DC measurements of the sensor under exposure to 1 ppm NO_2 . When investigated under 633 nm excitation, the Raman spectrum of MoS_2 exhibits several nonzone centers and second order peaks in addition to the zone-center E_{2g} and A_{1g} peak (Figure 4a). One of these is the longitudinal acoustic (LA) mode around 225 cm^{-1} , which is a Brillouin zone boundary (at the M and K points) phonon activated by defects. The intensity ratio of the LA mode to the E_{2g} and A_{1g} peaks can therefore be used as an indicator of the defect density.^[31,74] As shown in Figure 4a,b, the initial temperature of $100 \text{ }^\circ\text{C}$ was sufficient to reduce the defect densities by at least 40%, with further reduction in defect density observed throughout the stepwise annealing up until $400 \text{ }^\circ\text{C}$.

The intraflake resistance reached a maximum at $200 \text{ }^\circ\text{C}$ (Figure 4c) and reduced very slightly over the remainder of the temperature range. At this temperature, interflake resistance measurably reduced and DC sensitivity at 1 ppm was viable, indicating the existence of flake fusion and reduction

in interflake resistance. The flake-to-flake fusion resulted in an overall decrease in the actual baseline capacitance value due to an increase in connected surface area. An optimized sensor performance with the targeted $\Delta R_{\text{intra}}/R_{\text{intra}}$ is realized at after annealing at $200 \text{ }^\circ\text{C}$, corresponding to the R_{intra} baseline maximum, as the combination of decreased defect density and reduced adsorbents result in a $2\times$ improvement in sensor performance relative to the unannealed case. After $200 \text{ }^\circ\text{C}$, flake fusion begins to reduce edge sites for sensitivity, indicating that there presumably exists an optimal defect density/edge site configuration. Both R_{DC} and R_{inter} reduce to readable levels after this temperature (more information in Figure S7 in the Supporting Information).

The initial increase in R_{intra} suggests a reduction in charge carriers due to thermal annealing. In MoS_2 from natural materials, it has been observed that annealing to $350 \text{ }^\circ\text{C}$ increases native n-doping,^[75] which would reduce charge carrier density in a p-type material. Additionally, we attribute the p-type doping of these materials to excess adsorbed oxygen and such adsorbents are well-known to be expelled during annealing^[76] as evidenced by the reduction in defect density from Raman measurements. However, since the sensor never fully ceases to be p-type, it is unclear if residual oxygen remains after annealing at $400 \text{ }^\circ\text{C}$. Although some adsorbents can survive annealing,^[77] this suggests that oxygen is not merely occupying sulfur vacancies, but forming stable MoO_3 . XPS analysis of films before and after annealing indicate that the S:Mo⁺⁴ stoichiometry is not affected by the thermal treatment (i.e., expected 2:1 stoichiometry); however, the atomic abundance of Mo⁺⁶ decreases (i.e., MoO_3) suggesting removal of surface bound surface oxides (more details in Figure S13 in the Supporting Information).

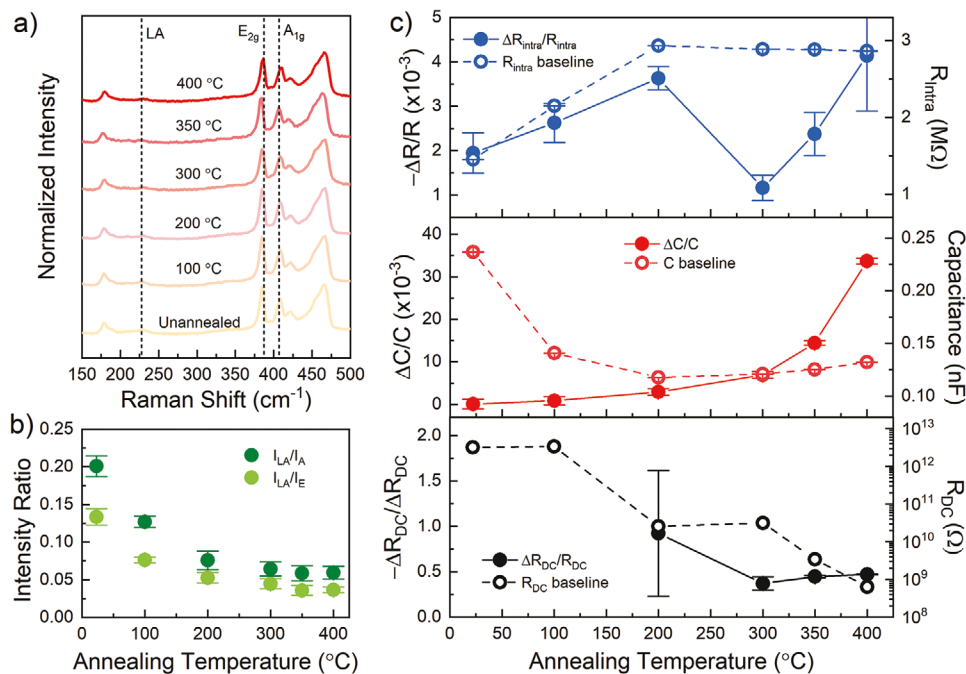


Figure 4. Influence of thermal annealing on defect density and sensor performance. a) Resonant Raman spectra at various annealing temperatures with b) defect densities as a function of annealing temperature based on the ratio of the LA mode intensity to the A_{1g} and E_{2g} modes, and c) sensor results under 1 ppm NO_2 for all circuit elements at different annealing conditions.

Previous studies suggest that the contribution from Schottky barriers should decrease with annealing in the range of 200–400 °C,^[78,79] which may explain the slight decline after 200 °C along with increased carrier mobility.^[80,81] Structural phase transitions to p-type MoS₂ have been observed at temperatures higher than 900 °C,^[82] which is far beyond the temperature range explored in this study. Clearly, the role of defects, doping, and flake-to-flake interactions are vital to the final sensor performance and are expected to play an important role in future real-time impedance sensing approaches with 2D nanoflakes.

The impedance approach developed under this work is generalizable to many other 2D material nanoflake configurations including WS₂ (see Figure S14 in the Supporting Information) and other TMD materials. Through accounting for variable RC constants expected in other nanoflake systems and further optimization of nanoflake film density, orientation, electronic properties, and thickness, improvement is expected for future gas sensing systems based on the as-described real-time impedance approach. Additionally, the equipment setup required to accumulate the data necessary for full frequency sweeps in real time is certainly hardware intensive, limiting the exact experimental configuration described here from being implemented into a low cost or wearable platform. However, the three-element circuit has only three degrees of freedom, and could theoretically be fitted with only two datapoints composed of magnitude and phase, allowing for a much simpler setup. Further optimization of materials so that only two or three select frequencies are required to fit the presented model could also reduce the required electronics to PCB-enabled or even wearable devices (further details can be found in Figure S15 in the Supporting Information).

3. Conclusions

Real-time impedance spectroscopy represents a unique gas sensor device methodology for solution-processed 2D materials that does not require any postprocessing and can be easily integrated onto flexible substrates. A three-element equivalent circuit fit enabled the impedance signal to independently monitor interflake (resistance and capacitance) and intraflake (resistance change due to doping) interactions. An empirical limit of detection of 1 ppb NO₂ was measured with an extrapolated ultimate detection limit of 63 ppt, all without the requirement of photoexcitation or gating. Moreover, this same device construct was demonstrated for an all solution-processed 2D sensor with printed graphene interconnects and a MoS₂ nanoflake channel on a polyimide substrate. A step-wise thermal annealing study revealed reduction in defect density in the MoS₂ nanoflake film with an increase in sensitivity by as much as 2× after annealing at 200 °C. Annealing at higher temperatures as high as 400 °C resulted in an increase in interflake interactions and a reduction in optimum sensor performance. The proposed impedance sensing modality, simple device configuration, and exceptional sensing performance in the described approach represents enticing flexible and effective sensor configuration for future chemical sensors built on 2D materials.

4. Experimental Section

Synthesis and Characterization of TMD Nanoflake Films: Further details regarding the synthesis and redox exfoliation of the nanoflake materials are described in ref. [29]. Briefly, the method utilized a redox cycle that generated polyoxometalates in solution that acted as an exfoliant to both delaminate layers from a bulk crystal via Coulombic repulsion and electrostatically stabilize the MoS₂.

XRD: XRD characterization patterns were recorded using a Rigaku Smartlab with Cu K α ($\lambda = 0.154$ nm) and obtained in $\theta/2\theta$ measurement mode. Thin films of TMDs were prepared via flow-coating (see Figure 1 for details) on Si substrates.

Atomic Force Microscopy (AFM): AFM samples were prepared via drop-casting dilute dispersions of MoS₂ flakes in acetonitrile (1×10^{-7} M) onto UVO treated Si wafer to improve solvent wettability. The samples were allowed to dry under ambient and subsequently annealed under vacuum (150 mTorr, 80 °C, 1 h) to ensure removal of all solvent to improve image quality. The samples were analyzed in a Bruker Dimension Icon in noncontact tapping mode utilizing an Al reflex coating cantilever (40 N m⁻¹). All images were analyzed utilizing the Nanoscope analysis software.

Device Fabrication: Sensor device configurations of Cr/Au electrodes (10 nm/100 nm thick) were evaporated onto a silicon wafer with a 150 nm SiO₂ overlayer using a patterned mask. Nanoflakes were then flow-coated using a glass blade, targeting 80 nm thickness, confirmed with a Bruker Dektak XTL profilometer. For the polyimide substrate, a graphene ink for aerosol jet printing (AJP) was prepared by first preparing graphene powder by a previously demonstrated method,^[83] which was then used to make a terpene/ethanol-based ink with further formulation and printing details in the Supporting Information.

Devices were enclosed in a Yamaichi STM8-QFP44 holder. The holder was placed in a stainless steel chamber. Analyte gas (10 and 1000 ppm NO₂ and NH₃ from Indiana Oxygen) was mixed with nitrogen to a total flow rate of 2000 sccm to target desired concentration. Mass flow controllers from MKS ranged from 20 to 2000 sccm. Liquid-sourced analytes were inundated with nitrogen in a glass bubbler, and the analyte concentration was calculated as saturated nitrogen at the measured temperature. See the Supporting Information for more details on the concentration calculations.

Sensor Measurement: DC measurements were taken with a Measurement Computing UB-1808X DAQ. AC measurements were taken with a Signal Recovery Model 7265 DSP lock-in amplifier. Initial measurements were optimized with a voltage divider using a high precision reference resistance. AC circuit elements were calculated from recorded frequency sweeps using a python script.

Supporting Information

Supporting Information is available from the Wiley Online Library or from the author.

Acknowledgements

N.R.G. acknowledges the support from the Air Force Office of Scientific Research grant FA9550-20RXCOR057. S.K. acknowledges the support from the Air Force Office of Scientific Research grant FA9550-20RHCOR040. Graphene powder production was supported by the National Science Foundation Scalable Nanomanufacturing Program (NSF CMMI-1727846 and NSF CMMI-2039268) and the National Science Foundation Future Manufacturing Program (NSF CMMI-2037026). S.G.W. and M.C.H. also acknowledge support from the U.S. Department of Commerce, National Institute of Standards and Technology (Award 70NANB19H005) as part of the Center for Hierarchical Materials Design (ChiMaD).

Conflict of Interest

The authors declare no conflict of interest.

Author Contributions

All authors contributed to the work presented.

Data Availability Statement

The data that support the findings of this study are available from the corresponding author upon reasonable request.

Keywords

2D materials, impedance spectroscopy, liquid phase exfoliation, molybdenum disulfide, sensors

Received: July 14, 2021

Revised: September 8, 2021

Published online:

- [1] N. R. Glavin, C. Muratore, M. Snure, *Oxford Open Mater. Sci.* **2020**, 1, itaa002.
- [2] A. Bolotsky, D. Butler, C. Dong, K. Gerace, N. R. Glavin, C. Muratore, J. A. Robinson, A. Ebrahimi, *ACS Nano* **2019**, 13, 9781.
- [3] T. Pham, G. Li, E. Bekyarova, M. E. Itkis, A. Mulchandani, *ACS Nano* **2019**, 13, 3196.
- [4] N. Yi, Z. Cheng, H. Li, L. Yang, J. Zhu, X. Zheng, Y. Chen, Z. Liu, H. Zhu, H. Cheng, *Mater. Today Phys.* **2020**, 15, 100265.
- [5] Y. Kim, S. Lee, J. G. Song, K. Y. Ko, W. J. Woo, S. W. Lee, M. Park, H. Lee, Z. Lee, H. Choi, W. H. Kim, J. Park, H. Kim, *Adv. Funct. Mater.* **2020**, 30, 2003360.
- [6] S. Yang, C. Jiang, S.-h. Wei, *Appl. Phys. Rev.* **2017**, 4, 021304.
- [7] M. G. Campbell, S. F. Liu, T. M. Swager, M. Dincă, *J. Am. Chem. Soc.* **2015**, 137, 13780.
- [8] S. Kanaparthi, S. G. Singh, *Mater. Sci. Energy Technol.* **2020**, 3, 91.
- [9] S. Kumar, V. Pavelyev, P. Mishra, N. Tripathi, P. Sharma, F. Calle, *Mater. Sci. Semicond. Process.* **2020**, 107, 104865.
- [10] R. Kumar, N. Goel, M. Kumar, *ACS Sens.* **2017**, 11, 1744.
- [11] W. Li, Y. Zhang, X. Long, J. Cao, X. Xin, X. Guan, J. Peng, X. Zheng, *Sensors* **2019**, 19, 2123.
- [12] Z. Meng, R. M. Stolz, L. Mendecki, K. A. Mirica, *Chem. Rev.* **2019**, 119, 478.
- [13] S. Ji, H. Wang, T. Wang, D. Yan, *Adv. Mater.* **2013**, 25, 1755.
- [14] D. Gu, X. Li, Y. Zhao, J. Wang, *Sens. Actuators, B* **2017**, 244, 67.
- [15] H. Long, A. Harley-Trochimczyk, T. Pham, Z. Tang, T. Shi, A. Zettl, C. Carraro, M. A. Worsley, R. Maboudian, *Adv. Funct. Mater.* **2016**, 26, 5158.
- [16] L. Yang, N. Yi, J. Zhu, Z. Cheng, X. Yin, X. Zhang, H. Zhu, H. Cheng, *J. Mater. Chem. A* **2020**, 8, 6487.
- [17] P. J. Cao, Y. Z. Cai, D. Pawar, S. T. Navale, C. N. Rao, S. Han, W. Y. Xu, M. Fang, X. K. Liu, Y. X. Zeng, W. J. Liu, D. L. Zhu, Y. M. Lu, *Chem. Eng. J.* **2020**, 401, 125491.
- [18] B. Sharma, A. Sharma, J.-h. Myung, *Sens. Actuators, B* **2021**, 331, 129464.
- [19] S. Zhao, Y. Shen, P. Zhou, X. Zhong, C. Han, Q. Zhao, D. Wei, *Sens. Actuators, B* **2019**, 282, 917.
- [20] A. Mukherjee, L. R. Jaidev, K. Chatterjee, A. Misra, *Nano Express* **2020**, 1, 010003.
- [21] B. Zong, Q. Li, X. Chen, C. Liu, L. Li, J. Ruan, S. Mao, *ACS Appl. Mater. Interfaces* **2020**, 12, 50610.
- [22] Y. Hong, W. M. Kang, I. T. Cho, J. Shin, M. Wu, J. H. Lee, *J. Nanosci. Nanotechnol.* **2017**, 17, 3151.
- [23] Q. He, Z. Zeng, Z. Yin, H. Li, S. Wu, X. Huang, H. Zhang, *Small* **2012**, 8, 2994.
- [24] M. Mathew, C. S. Rout, *J. Mater. Chem. C* **2021**, 9, 395.
- [25] Y. Kim, S. K. Kang, N. C. Oh, H. D. Lee, S. M. Lee, J. Park, H. Kim, *ACS Appl. Mater. Interfaces* **2019**, 11, 38902.
- [26] G. Neri, *Chemosensors* **2017**, 5, 21.
- [27] H. Hashtroudi, I. D. R. MacKinnon, M. Shafiei, *J. Mater. Chem. C* **2020**, 8, 13108.
- [28] H. Wang, L. Zhou, Y. Liu, F. Liu, X. Liang, F. Liu, Y. Gao, X. Yan, G. Lu, *Sens. Actuators, B* **2020**, 305, 127498.
- [29] B. Liu, L. Chen, G. Liu, A. N. Abbas, M. Fathi, C. Zhou, *ACS Nano* **2014**, 5, 5304.
- [30] G. Chen, T. M. Paronyan, A. R. Harutyunyan, *Appl. Phys. Lett.* **2012**, 101, 053119.
- [31] R. Rao, V. Carozo, Y. Wang, A. E. Islam, N. Perea-Lopez, K. Fujisawa, V. H. Crespi, M. Terrones, B. Maruyama, *2D Mater.* **2019**, 6, 045031.
- [32] H. Tabata, H. Matsuyama, T. Goto, O. Kubo, M. Katayama, *ACS Nano* **2021**, 15, 2542.
- [33] W. Zheng, Y. Xu, L. Zheng, C. Yang, N. Pinna, X. Liu, J. Zhang, *Adv. Funct. Mater.* **2020**, 30, 2000435.
- [34] G. L. Frey, K. J. Reynolds, R. H. Friend, *Adv. Mater.* **2002**, 14, 265.
- [35] D. Butler, D. Moore, N. R. Glavin, J. A. Robinson, A. Ebrahimi, *ACS Appl. Mater. Interfaces* **2021**, 13, 11185.
- [36] X. Liu, T. Ma, N. Pinna, J. Zhang, *Adv. Funct. Mater.* **2017**, 27, 1702168.
- [37] Y. B. Kim, S. H. Jung, D. S. Kim, N. G. Deshpande, H. W. Suh, H. H. Lee, J. H. Choi, H. S. Lee, H. K. Cho, *Adv. Funct. Mater.* **2021**, 31, 2102439.
- [38] T. Yun, H. M. Jin, D. H. Kim, K. H. Han, G. G. Yang, G. Y. Lee, G. S. Lee, J. Y. Choi, I. D. Kim, S. O. Kim, *Adv. Funct. Mater.* **2018**, 28, 1804508.
- [39] A. J. Bard, L. R. Faulkner, *Electrochemical Methods: Fundamentals and Applications*, 2nd ed., John Wiley & Sons, Ltd, New York **2001**.
- [40] F. Ciucci, *Curr. Opin. Electrochem.* **2019**, 13, 132.
- [41] J. Muñoz, R. Montes, M. Baeza, *TrAC, Trends Anal. Chem.* **2017**, 97, 201.
- [42] J. R. Scully, D. C. Silverman, *Electrochemical Impedance: Analysis and Interpretation*, ASTM International, West Conshohocken, PA **1993**.
- [43] L. Y. Woo, L. P. Martin, R. S. Glass, W. Wang, S. Jung, R. J. Gorte, E. P. Murray, R. F. Novak, J. H. Visser, *J. Electrochem. Soc.* **2008**, 155, J32.
- [44] L. P. Martin, L. Y. Woo, R. S. Glass, *J. Electrochem. Soc.* **2007**, 154, J97.
- [45] H. C. Cho, S. Takase, J. H. Song, Y. Shimizu, *Sens. Actuators, B* **2013**, 187, 94.
- [46] C. C. Mayorga-Martinez, Z. Sofer, M. Pumera, *Angew. Chem., Int. Ed.* **2015**, 54, 14317.
- [47] M. A. Al Mamun, M. R. Yuce, *Adv. Funct. Mater.* **2020**, 30, 2005703.
- [48] A. Jawaid, D. Nepal, K. Park, M. Jespersen, A. Qualley, P. Mirau, L. F. Drummy, R. A. Vaia, *Chem. Mater.* **2016**, 28, 337.
- [49] A. Jawaid, J. Che, L. F. Drummy, J. Bultman, A. Waite, M. S. Hsiao, R. A. Vaia, *ACS Nano* **2017**, 11, 635.
- [50] A. M. Jawaid, A. J. Ritter, R. A. Vaia, *Chem. Mater.* **2020**, 32, 6550.
- [51] D. Dutta, A. Oz, O. Hod, E. Koren, *Nat. Commun.* **2020**, 11, 4746.
- [52] C. N. R. Rao, K. Gopalakrishnan, U. Maitra, *ACS Appl. Mater. Interfaces* **2015**, 7, 7809.
- [53] A. B. Kaiser, C. Gómez-Navarro, R. S. Sundaram, M. Burghard, K. Kern, *Nano Lett.* **2009**, 9, 1787.
- [54] H. Qiu, T. Xu, Z. Wang, W. Ren, H. Nan, Z. Ni, Q. Chen, S. Yuan, F. Miao, F. Song, G. Long, Y. Shi, L. Sun, J. Wang, X. Wang, *Nat. Commun.* **2013**, 4, 2642.

- [55] J. Xue, S. Huang, J.-Y. Wang, H. Q. Xu, *RSC Adv.* **2019**, *9*, 17885.
- [56] K. Huang, M. Zhao, B. Sun, X. Liu, J. Liu, H. Chang, Y. Zeng, H. Liu, *ACS Appl. Electron. Mater.* **2020**, *2*, 971.
- [57] R. Negishi, M. Akabori, T. Ito, Y. Watanabe, Y. Kobayashi, *Sci. Rep.* **2016**, *6*, 28936.
- [58] N. T. Thang, L. T. Hong, N. H. Thoan, C. M. Hung, N. Van Duy, N. Van Hieu, N. D. Hoa, *RSC Adv.* **2020**, *10*, 12759.
- [59] K. Dolui, I. Rungger, S. Sanvito, *Phys. Rev. B: Condens. Matter Mater. Phys.* **2013**, *87*, 165402.
- [60] A. T. Neal, R. Pachter, S. Mou, *Appl. Phys. Lett.* **2017**, *110*, 193103.
- [61] R. Rao, H. Kim, N. Perea-López, M. Terrones, B. Maruyama, *Nanoscale* **2021**, *13*, 11470.
- [62] W. Zhou, X. Zou, S. Najmaei, Z. Liu, Y. Shi, J. Kong, J. Lou, P. M. Ajayan, B. I. Yakobson, J. C. Idrobo, *Nano Lett.* **2013**, *13*, 2615.
- [63] D. Liu, Y. Guo, L. Fang, J. Robertson, *Appl. Phys. Lett.* **2013**, *103*, 183113.
- [64] D. Le, T. B. Rawal, T. S. Rahman, *J. Phys. Chem. C* **2014**, *118*, 5346.
- [65] D. Kiriya, Y. Zhou, C. Nelson, M. Hettick, S. R. Madhvapathy, K. Chen, P. Zhao, M. Tosun, A. M. Minor, D. C. Chrzan, A. Javey, *Adv. Funct. Mater.* **2015**, *25*, 6257.
- [66] C. Gong, L. Colombo, R. M. Wallace, K. Cho, *Nano Lett.* **2014**, *14*, 1714.
- [67] P. Bampoulis, R. Van Bremen, Q. Yao, B. Poelsema, H. J. W. Zandvliet, K. Sotthewes, *ACS Appl. Mater. Interfaces* **2017**, *9*, 19278.
- [68] Y. Guo, D. Liu, J. Robertson, *Appl. Phys. Lett.* **2015**, *106*, 173106.
- [69] K. A. Min, J. Park, R. M. Wallace, K. Cho, S. Hong, *2D Mater.* **2017**, *4*, 015019.
- [70] Y. Guo, D. Liu, J. Robertson, *ACS Appl. Mater. Interfaces* **2015**, *46*, 25709.
- [71] E. S. R. Bovill, J. Griffin, T. Wang, J. W. Kingsley, H. Yi, A. Iraqi, A. R. Buckley, D. G. Lidzey, *Appl. Phys. Lett.* **2013**, *102*, 183303.
- [72] H. Hashtroudi, P. Atkin, I. D. R. Mackinnon, M. Shafei, *Int. J. Hydrogen Energy* **2019**, *44*, 26646.
- [73] O. Redlich, D. L. Peterson, *J. Phys. Chem.* **1959**, *63*, 1024.
- [74] S. Mignuzzi, A. J. Pollard, N. Bonini, B. Brennan, I. S. Gilmore, M. A. Pimenta, D. Richards, D. Roy, *Phys. Rev. B: Condens. Matter Mater. Phys.* **2015**, *91*, 195411.
- [75] B. W. H. Baugher, H. O. H. Churchill, Y. Yang, P. Jarillo-Herrero, *Nano Lett.* **2013**, *13*, 4212.
- [76] J. R. Durán Retamal, D. Periyangounder, J. J. Ke, M. L. Tsai, J. H. He, *Chem. Sci.* **2018**, *9*, 7727.
- [77] Y. Wang, A. Slassi, M. A. Stoeckel, S. Bertolazzi, J. Cornil, D. Beljonne, P. Samorì, *J. Phys. Chem. Lett.* **2019**, *10*, 540.
- [78] H. C. P. Movva, A. Rai, S. Kang, K. Kim, B. Fallahzad, T. Taniguchi, K. Watanabe, E. Tutuc, S. K. Banerjee, *ACS Nano* **2015**, *9*, 10402.
- [79] D. Qi, Q. Wang, C. Han, J. Jiang, Y. Zheng, W. Chen, W. Zhang, A. T. S. Wee, *2D Mater.* **2017**, *4*, 045016.
- [80] H. Xu, H. Zhang, Y. Liu, S. Zhang, Y. Sun, Z. Guo, Y. Sheng, X. Wang, C. Luo, X. Wu, J. Wang, W. Hu, Z. Xu, Q. Sun, P. Zhou, J. Shi, Z. Sun, D. W. Zhang, W. Bao, *Adv. Funct. Mater.* **2019**, *29*, 1805614.
- [81] S. Ahmed, J. Yi, *Nano-Micro Lett.* **2017**, *9*, 50.
- [82] R. Mukherjee, H. J. Chuang, M. R. Koehler, N. Combs, A. Patchen, Z. X. Zhou, D. Mandrus, *Phys. Rev. Appl.* **2017**, *7*, 034011.
- [83] Y. T. Liang, M. C. Hersam, *J. Am. Chem. Soc.* **2010**, *132*, 17661.